A statistical study of the inner edge of the electron plasma sheet and the net convection potential as a function of geomagnetic activity

F. Jiang,[1,2] M. G. Kivelson,[1,3] R. J. Walker,[1,2] K. K. Khurana,[1] V. Angelopoulos,[1,2] and T. Hsu[1]

Received 5 October 2010; revised 21 February 2011; accepted 1 April 2011; published 25 June 2011.

[1] A widely accepted explanation of the location of the inner edge of the electron plasma sheet and its dependence on electron energy is based on drift motions of individual particles. The boundary is identified as the separatrix between drift trajectories linking the tail to the dayside magnetopause (open paths) and trajectories closed around the Earth. A statistical study of the inner edge of the electron plasma sheet using THEMIS Electrostatic Analyzer plasma data from November 2007 to April 2009 enabled us to examine this model. Using a dipole magnetic field and a Volland-Stern electric field with shielding, we find that a steady state drift boundary model represents the average location of the electron plasma sheet boundary and reflects its variation with the solar wind electric field in the local time region between 21:00 and 06:00, except at high activity levels. However, the model does not reproduce the observed energy dispersion of the boundaries. We have also used the location of the inner edge of the electron plasma sheet to parameterize the potential drop of the tail convection electric field as a function of solar wind electric field (E_{sw}) and geomagnetic activity. The range of E_{sw} examined is small because the data were acquired near solar minimum. For the range of values tested (meaningful statistics only for $E_{sw} < 2$ mV/m), reasonably good agreement is found between the potential drop of the tail convection electric field inferred from the location of the inner edge and the polar cap potential drop calculated from the model of Boyle et al. (1997).

Citation: Jiang, F., M. G. Kivelson, R. J. Walker, K. K. Khurana, V. Angelopoulos, and T. Hsu (2011), A statistical study of the inner edge of the electron plasma sheet and the net convection potential as a function of geomagnetic activity, *J. Geophys. Res.*, *116*, A06215, doi:10.1029/2010JA016179.

1. Introduction

[2] Observations of the electron flux distribution in the inner magnetosphere date back to the early 1960s. Observations from the OGO 1 and OGO 3 spacecraft indicated that the electron plasma sheet is terminated on the earthward side by a well-defined sharp boundary in the local time region from 17:00 to 22:00 [*Vasyliunas*, 1968]. *Frank* [1971] found that this earthward edge of the electron plasma sheet is at 6–8 R_E in the postmidnight sector (from 00:00 to 03:00 magnetic local time (MLT)) and 7–8 R_E in the premidnight sector (21:00–00:00 MLT) at the magnetic equator during periods of relative magnetic quiescence. Another important observation is that the boundaries of lower-energy plasma sheet electrons are often closer to the Earth than those of higher energies [*Schield and Frank*, 1970; *Frank*, 1971]. More recently, a statistical survey fluxes of particles with energies from ~1 eV to ~30 keV based on a year of data from Los Alamos geosynchronous satellites showed distinct inner boundaries of the electron fluxes. When displayed as a function of *Kp* and MLT, it was found that as *Kp* increases, this boundary moves earthward and the satellites at geosynchronous altitude may be immersed in hot plasma sheet electrons [*Korth et al.*, 1999].

[3] Several theories have been proposed to explain these observations. A widely accepted one is based on the drift motion of individual particles. Particle drift patterns are principally determined by the collective effects of earthward convection, co-rotation and magnetic gradient and curvature drift that are controlled by the magnetic field and global electric field configurations in the inner magnetosphere. The inner boundary of the plasma sheet is the separatrix between trajectories of particles that reach the middle and/or inner magnetosphere from sources in the plasma sheet and trajectories of particles that drift on closed paths around the Earth [*Alfvén and Falthammar*, 1963; *Chen*, 1970; *Kivelson and Southwood*, 1975]. *Korth et al.* [1999] compared electron flux cutoffs measured by geosynchronous satellites with separatrices between open and closed drift trajectories

[1]Institute of Geophysics and Planetary Physics, University of California, Los Angeles, California, USA.
[2]Department of Earth and Space Sciences, University of California, Los Angeles, California, USA.
[3]Department of Atmospheres, Oceans, and Space Sciences, University of Michigan, Ann Arbor, Michigan, USA.

0148-0227/11/2010JA016179

calculated by a Hamiltonian energy conservation approach [*Whipple*, 1978] using a *Kp*-dependent electric field model. They found good agreement between the observational boundaries and theoretical positions in the local time region from 20:00 to 05:00. *Friedel et al.* [2001] expanded their results to cover the entire inner magnetosphere by using data from the Polar HYDRA instrument projected to an equatorial reference plane, and they also found that the inner boundaries of plasma sheet electrons are well organized by simple theoretical Alfvén boundaries on the nightside.

[4] Particle drift paths seem often to account for the structure of the inner edge of the electron plasma sheet, but other processes, both quasi-steady and dynamic, may also contribute. *Kerns et al.* [1994] used low-energy plasma analyzer data collected by the CRRES satellite over a 14 month period to examine how often a simple convection model can explain the structure seen in 120 eV to 28 keV particles at the inner edge of the plasma sheet. They found that 40%–50% of the cutoffs sampled on the nightside were consistent with those derived from a convection model with one variable. The model was often inconsistent with cutoffs measured during increasing activity and with those measured on the dayside.

[5] Electron loss through precipitation is known to be a factor that contributes to the inconsistency between observed boundaries and those described by the drift boundary model. *Kennel* [1969] introduced the concept of a flow-precipitation boundary and suggested that strong precipitation would create a boundary to the plasma sheet at the location where the convective flow time and minimum life time of strong pitch angle diffusion become comparable. *Korth et al.* [1999] and *Friedel et al.* [2001] both found that electrons at all energies show increasing losses as they drift toward dayside, but no quantitative comparison between observations and a precipitation boundary model has been conducted.

[6] In contrast with the steady state drift boundary models discussed above, an alternative view provided by *Mauk and Meng* [1983] related the inner boundary of the plasma sheet to dynamic injections. They proposed that particles are injected sporadically from an "injection boundary" on the nightside. Following the long-term evolution of these injected particles, they found that many signatures that cannot be obtained from the steady state model were reproduced in their dynamic injection model. The Mauk and Meng model assumes injection over a broad range of local times on the nightside of the magnetosphere. Such injections are likely to be associated with substorm expansion, and hence to occur during intervals of enhanced activity.

[7] It is well established that intermittent injections at high radial speeds occur over limited angular ranges as bursty bulk flows (BBF) [*Angelopoulos et al.*, 1992, 1994] even during relatively quiet times. The influence of BBFs on the location of the inner edge of the plasma sheet may be primarily to increase the scatter about an averaged location and to move the measured averaged boundary inward. Furthermore, the flux cutoffs resulting from dynamic injection is approximately dispersionless, so the effect of BBFs on the average positions should be to decrease the separations of boundaries at different energies.

[8] The THEMIS mission, which deployed five identical microsatellites equipped with comprehensive particle instruments, provides a data set that can usefully extend studies of the inner plasma sheet [*Angelopoulos*, 2008]. The three inner THEMIS probes cover a radial range from ~2 R_E to 12 R_E at all local times near the equatorial plane. With three spacecraft available to identify plasma boundaries, our statistical database is much more extensive than previous observational bases. In the next section, we introduce the THEMIS instrumentation from which our data are obtained, describe our data selection, and show an example of how the location of the inner boundary of the electron plasma sheet is obtained from particle flux measurements. As the data to be used for analysis are acquired at fixed energies, the model of the steady state drift boundary for particles of fixed energy, based on the work of *Southwood and Kivelson* [1975], is introduced in section 3. Section 4 displays the statistical results of the location of the inner edge of the electron plasma sheet on the nightside and its variation with geomagnetic activity and electron kinetic energy. Section 5 presents our parameterization of potential drop of the tail convection electric field inferred from the location of the cutoff boundary, and we relate our statistical results to indicators of geomagnetic activity and to models of the cross polar cap potential. Our study is discussed and summarized in section 6 where we relate our statistical results to indicators of geomagnetic activity and to models of the polar cap potential drop.

2. Data

[9] This study uses Electrostatic Analyzer (ESA) plasma data from the three inner THEMIS spacecraft (THEMIS A, D, and E) from November 2007 to April 2009 to identify the inner edge of the electron plasma sheet as a function of electron energy. Because the trajectories become increasingly azimuthal in the vicinity of the inner edge for orbits with apogees near dusk and the boundary cutoffs become difficult to identify, we focus on the boundary crossings from 21:00 to 06:00 in MLT where the spacecraft trajectories cross the inner edge of the plasma sheet at reasonably small angles relative to the radial direction [*Sibeck and Angelopoulos*, 2008].

[10] The energy range of the ESA (Electrostatic Analyzer) instrument on a THEMIS spacecraft extends from ~5 eV to ~30 keV and is divided into 32 energy channels [*McFadden et al.*, 2008]. We used only the 10 energy channels that record the typical energy range for plasma sheet electrons (0.7–9 keV) for our study. The penetrating radiation contamination is removed from the electron ESA spectrum by subtracting the minimum E_{flux} (omnidirectional differential electron energy flux) value through all the energy bins [*McFadden et al.*, 2008]. The background subtraction technique removes most of the penetrating radiation contamination but still leaves residual flux in the spectrum (indicated by the magenta rectangles in Figure 1b). Usually, there is an identifiable gap between the inner edge of the electron plasma sheet and the residual flux of background contamination (as indicated in Figures 1a–1c). Sometimes, the cutoff boundary is embedded within the residual flux from the penetrating radiation contamination, but the intensity of the latter is very small compared with the plasma sheet fluxes and the boundary can still be identified. We exclude the cases only when the cutoff boundary cannot be distinguished from the residual flux of penetrating radiation contamination (these cases comprise less than 10% of our events). Figure 2 is such an example. The spacecraft moves radially inward and encounters the slot

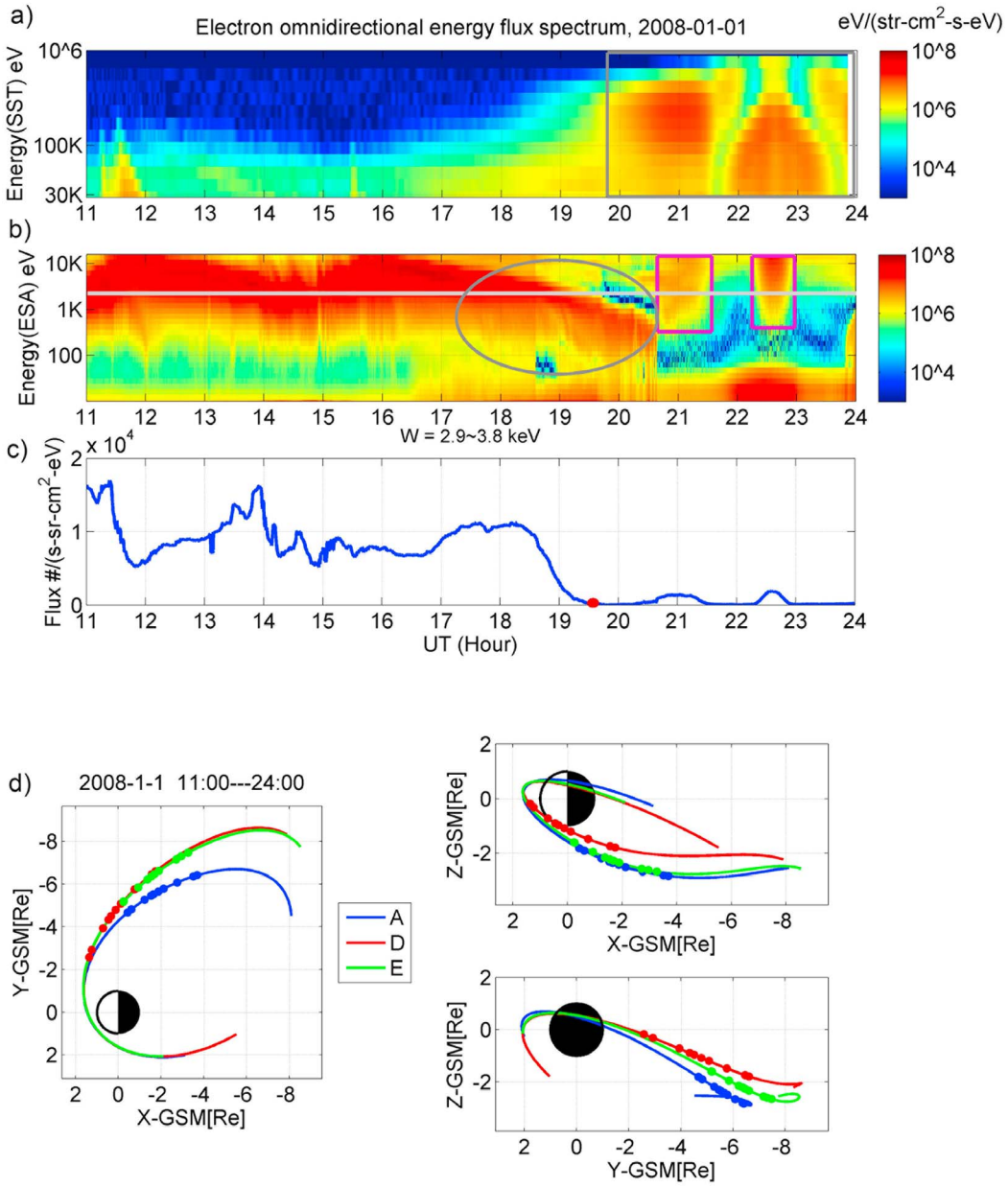

Figure 1. (a) Solid State Telescopes (SST) and (b) Electrostatic Analyzers electron energy flux spectrum versus UT measured by THEMIS A on an inbound pass on 1 January 2008. The electron radiation belt is indicated by the shaded rectangle, and the inner edge of the electron plasma sheet is indicated by the shaded oval on the inbound segment of the orbit. The penetrating radiation contamination has been removed from the electron ESA spectrum, and the residual contamination fluxes after we subtract background are indicated by the magenta rectangles. The shaded line indicates the energy bin of 2.9~3.8 keV. (c) Omnidirectional differential flux of electrons at the energies from 2.9 to 3.8 keV versus UT. The red dot indicates the time THEMIS A encounters 2.9 keV electrons' cutoff boundary. (d) Spacecraft trajectories of THEMIS A, D, and E in GSM coordinates in the *XY*, *YZ*, and *XZ* planes for this event. The dots mark the cutoff boundaries of different energies, and the most distant ones correspond to the highest energy.

region (slightly after 20:00 UT) and the inner radiation belt (~20:20 UT) with closest approach around 21:00 UT (1.5 R_E). The cutoff boundary of 10 keV electrons (the energy is marked by the shaded line in Figure 2) overlaps with the residual flux of background radiation) and cannot be identified. Therefore, this event is not included in our data set.

[11] In order to facilitate processing of the large data set, an algorithm is applied to identify the boundary crossings. Figures 1a–1c illustrate how the algorithm works. Figures 1a and 1b show the omnidirectional differential electron energy flux spectrum versus UT measured by Solid State Telescopes (SST) and Electrostatic Analyzers (ESA) from THEMIS A on

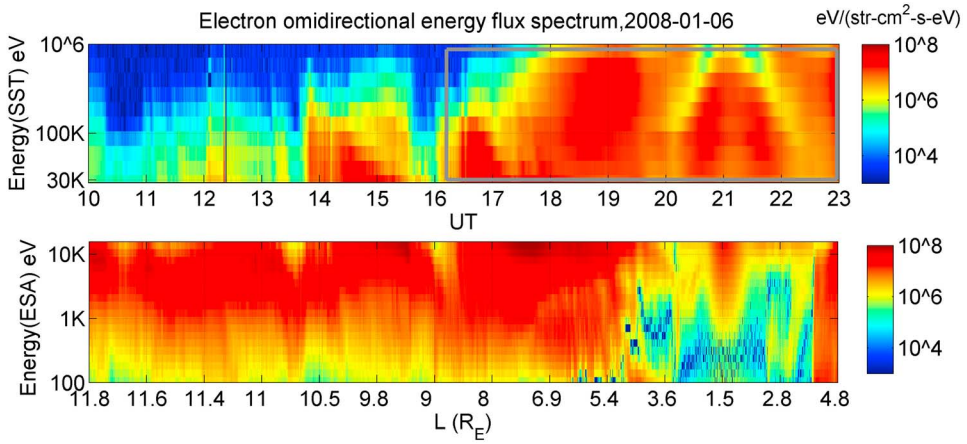

Figure 2. Electron energy flux spectrum versus UT measured by THEMIS D on an inbound pass on 6 January 2008. This is a case where the cutoff boundary of the electron plasma sheet is embedded within the residual flux of the penetrating radiation contamination and cannot be identified.

an inbound pass on 1 January 2008. The part of the electron radiation belt where the flux intensity peaks is indicated by the shaded rectangle, and the inner edge of the electron plasma sheet is indicated by the shaded oval on the inbound segment of the orbit. We obtain the differential electron flux versus UT for each energy bin from the energy flux spectrum and then detrend the time series via a 3 min moving-average filter. Figure 1c plots the omnidirectional differential flux versus UT for electrons in the energy bin from 2.9 to 3.8 keV, the energy range just above the lightly shaded line that has been superimposed on the spectrogram of Figure 1a. The red dot at the bottom edge of the slope near 19:20 UT, which corresponds to termination of the flux decrease, is chosen as the flux cutoff of 2.9 keV electrons (2.9 keV is the lower end of the energy bin, which extends from 2.9 keV to 3.8 keV). Figure 1d shows trajectories of THEMIS A, D, and E in GSM coordinates in the *XY*, *YZ*, and *XZ* planes for this event. The dots mark the cutoff boundaries of different energies, and the most distant ones correspond to the highest energy. For the inbound portion of the spacecraft orbit, the algorithm first identifies the electron inner radiation belt (the electron radiation belt appears as three discontinuous intervals of enhanced fluxes observed in the SST energy flux spectrum near perigee) and then traces backward in time to look for the first large flux gradient encountered by the spacecraft (evident in Figure 1c as a flux drop prior to 20:00 UT) in a particular energy channel. Then the algorithm identifies the lowest point on the steep gradient as the boundary cutoff of electrons with energy equal to the lower bound of that energy bin.

[12] After running the algorithm on the entire data set, we check all the results by eye to eliminate those cases incorrectly picked up by the code. Mistakenly selected cases occur in the following situations: (1) Flux variation occurs because the spacecraft traverses the plasma sheet in the north-south direction and enters the lobe and (2) highly fluctuating electron fluxes are observed simultaneously with observation of strong wave activity in the electric field. We exclude such cases because the flux variation may be a result of wave scattering instead of boundary crossing. For the events where multiple flux cutoffs are observed in a single pass, we select the cutoff closest to the Earth as the inner edge. It is worth noting that there is not always a monotonic change of boundary cutoff versus energy, and the structure of the boundary can be very complicated. It is likely that complex boundary structure is observed when a dynamic boundary is produced in response to variable flows, injections, magnetic field reconfigurations, etc. We include these events in our database because we are seeking to establish whether, even in the presence of temporal variations, a steady state drift boundary model can account for average location of the inner boundary.

3. The Steady State Drift Boundary Model

[13] *Alfvén and Falthammar* [1963] introduced the concept of a separatrix between open and closed drift trajectories of particles of a given magnetic moment μ. The separatrix is now referred to as an Alfvén layer. Satellites, however, do not measure μ directly; they measure particle kinetic energy W instead. For this reason, *Kivelson and Southwood* [1975] modified the underlying equations to provide the locus where the cutoff boundary would be encountered by a spacecraft measuring electrons at energy W. We apply their procedure here and assume that the magnetic field is a dipole field but replace the uniform electric field of their work with the Volland-Stern electric field model [*Volland*, 1973; *Stern*, 1975], which has the following form:

$$U(r,\phi) = -\frac{C}{r} + br^{\gamma}\sin\phi, \tag{1}$$

where b describes the strength of the cross-tail convection electric field. The angle ϕ is magnetic local time (measured in radians) with origin at midnight, increasing counterclockwise, $C = 92.4$ kV is the co-rotation electric potential, γ is the shielding factor; $\gamma = 2$ is the typical value adopted in literature to describe the degree of shielding, but we take it as a parameter to be determined. When $\gamma = 1$, the convection electric field becomes a uniform dawn to dusk electric

field. The total energy of a particle on the magnetic equatorial plane is

$$W_{\mathrm{tot}} = W + qbR_E^{\gamma}L^{\gamma}\sin\phi - \frac{qC}{L}(r = L^{*}R_E). \tag{2}$$

The total energy (kinetic plus potential) is conserved along a particle drift path. L is radial distance to the Earth in R_E measured at the equator. Variable q is the electric charge of a particle. The separatrix between the hot tenuous electron plasma sheet and the cold electrons that rotate around the Earth is a member of a family of surfaces composed of the field lines whose equatorial loci are the equipotential contours that pass through the stagnation point, where the drift velocity $\mathbf{v}_s = 0$ (the bounce averaged drift velocity can be written as $\mathbf{v}_s = [-\nabla(W_{\mathrm{tot}}/\mathrm{q}) \times \mathbf{B}]/B^2$), i.e.,

$$\frac{\partial W_{\mathrm{tot}}}{\partial L}|_s = 0 \quad , \frac{\partial W_{\mathrm{tot}}}{\partial \phi}|_s = 0;$$

thus,

$$\begin{cases} \dfrac{\partial W}{\partial L}|_s + qb\sin\phi \mathrm{R}_E^{\gamma}\gamma L^{\gamma-1} + \dfrac{qC}{L^2} = 0 \\ \cos\phi_s = 0 \end{cases}. \tag{3}$$

The variation of W with L for adiabatic transport is approximated by *Southwood and Kivelson* [1975] as

$$\frac{W}{W_s} = \left(\frac{L_s}{L}\right)^{\nu}, \nu = 2.1 + 0.9\sin\alpha_{\mathrm{eqs}}, \tag{4}$$

where α_{eqs} is equatorial pitch angle of a particle. A subscript s is used to identify the value of the parameter at the stagnation point. For electrons, $q = -e$, $\phi_s = 3\pi/2$, so at the stagnation point,

$$\nu W_s = -eb\sin\phi_s \mathrm{R}_E^{\gamma}\gamma L_s^{\gamma} - \frac{eC}{L_s}. \tag{5}$$

Because the total energy is conserved along the electron's orbit that passes through the stagnation point, it follows that

$$W - ebR_E^{\gamma}L^{\gamma}\sin\phi + \frac{eC}{L} = W_s - ebR_E^{\gamma}L_s^{\gamma}\sin\phi_s + \frac{eC}{L_s} \tag{6}$$

$$\frac{W}{W_s} = \left(\frac{L_s}{L}\right)^{\nu}. \tag{7}$$

There are three equations with three unknown variables: W_s, L, L_s. For given values of ν, W, ϕ, we can solve the equations numerically to obtain L as a function of ϕ.

[14] Once we solve the equations of L for given ν, W, ϕ, and the convection strength b, the configuration of the drift boundary is known. Figure 3a shows models of the cutoff boundaries between open and closed drift paths of equatorially mirroring ($\alpha_0 = 90°$, $\nu = 3.0$) electrons of different kinetic energies in the magnetic equatorial plane. Figure 3b shows the equatorial cutoff boundaries of 4 keV electrons with different equatorial pitch angles ($\alpha_{\mathrm{eqs}} = 0°, 45°, 90°$) at the stagnation point. The model leads to a teardrop-shaped cutoff boundary that is asymmetric about the noon-midnight meridian. The dotted lines correspond to the case of a uniform convection electric field ($\gamma = 1$), and the solid lines correspond to the case of a shielded convection electric field ($\gamma = 2$) in the inner magnetosphere. The values of b are chosen so that the potential drop across the magnetosphere in the dawn-dusk median is 50 kV for both cases (the electric field is integrated across 25 R_E in the y direction). The cutoff boundary resulting from a shielded convection electric field is more circular than that from a uniform convection field, especially on the dusk side. For either form of electric field, the cutoff boundary of low-energy electrons lies well within that of high-energy electrons. In addition, the more field aligned the electrons are, the more earthward their boundary lies, although the differences resulting from different initial pitch angles are quite inconspicuous except on the dusk side. Because the separation between cutoff boundaries of electrons of the same energy but different initial pitch angles is quite small in the local time region on which we will focus, hereafter we set $\nu = 3.0$ in the model, thereby using the cutoff boundary of equatorially mirroring electrons to represent the boundary of electrons with arbitrary pitch angle. Figure 3c shows the cutoff boundaries of equatorially mirroring electrons (4 keV) for different degrees of shielding (γ) of the convection electric field. One can see that, for the same potential drop across the magnetosphere, as the degree of shielding decreases, plasma sheet electrons penetrate closer to the Earth.

4. Statistical Results

[15] The drift boundary model we discussed above describes an inner edge of the electron plasma sheet dependent on electron kinetic energy and the convection electric field. In this section, we organize our data set of the flux cutoff by electron kinetic energy and solar wind electric field E_y to see if the inner edge does depend on these quantities and whether, given appropriately chosen parameters, their relations can be reproduced by the drift boundary model.

4.1. Variation of the Boundary Location With Electron Kinetic Energy

[16] Typically, a spacecraft inbound through the plasma sheet on the nightside at quiet times observes sharp decreases of electron flux first at high energies and later at lower energies, whereas a spacecraft outbound observes sudden enhancement of electron flux first at lower energies and later at higher energies. This structure appears as a gradual slope in the electron energy flux dynamic spectrum (Figure 1b) and is referred to as a dispersive boundary. The explanation for a dispersive boundary is that the electron gradient and curvature drift speed is proportional to the electron kinetic energy and inversely proportional to L, so the azimuthal drift velocity component that diverts the flow is larger for hot electrons than for cold electrons at the same location. Therefore, hot electrons start to drift azimuthally at a larger radial distance and form a cutoff boundary outward of that of the low-energy electrons. Sometimes a spacecraft observes the cutoff boundaries simultaneously at all energies, and this is referred to as a dispersionless boundary. Dispersionless signatures are common at disturbed times and are usually attributed to rapid motion of the boundary or dynamic injection.

[17] Figure 4 displays the equatorial radial distance of the electron cutoff boundary L versus kinetic energy E_k at

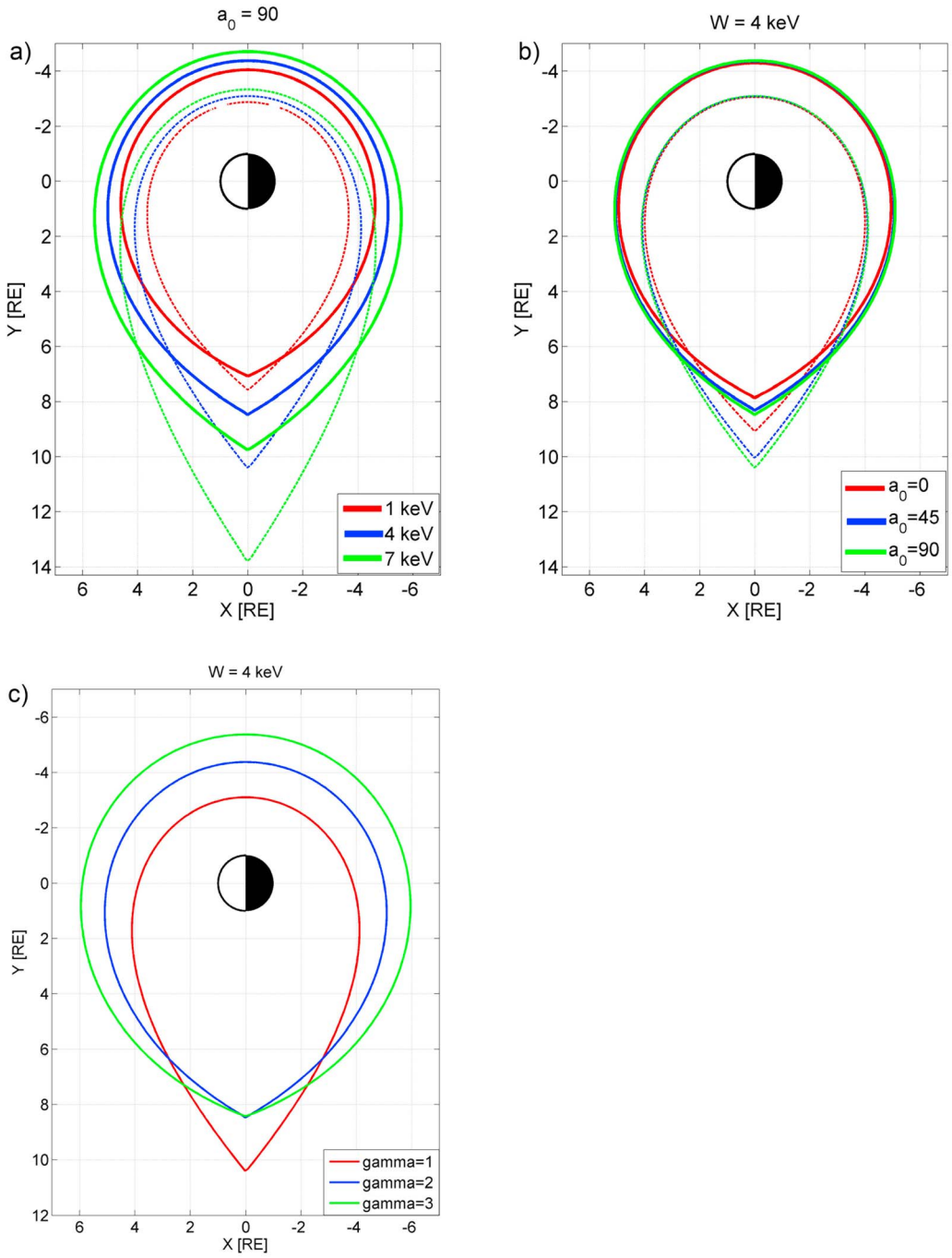

Figure 3. Equatorial electron cutoff boundaries calculated from the drift boundary model by using two different electric field models and a dipole magnetic field. The contours plotted as solid lines correspond to the Volland-Stern electric field ($\gamma = 2$). The dotted lines correspond to the case of a uniform cross-tail electric field where $\gamma = 1$. The cross-tail potential drop is 50 kV for both cases here. (a) Boundaries for electrons of different kinetic energies. (b) Boundaries for 4 keV electrons with different equatorial pitch angles at the stagnation point at dusk. (c) Boundaries of 4 keV electrons for different degrees of shielding (γ) in the Volland-Stern electric field model.

different MLTs between 22:00 and 06:00, for different levels of activity as characterized by the *AE* index. Again locations of the flux cutoffs are mapped to the magnetic equator along a dipole magnetic field to obtain the *L* shell value. Black dots and error bars are the means and SEMs (standard error of the mean, which is the standard deviation divided by $\sqrt{N}$, where N is the number of samples) of *L* in each energy channel. The red curves are the values calculated from the drift boundary

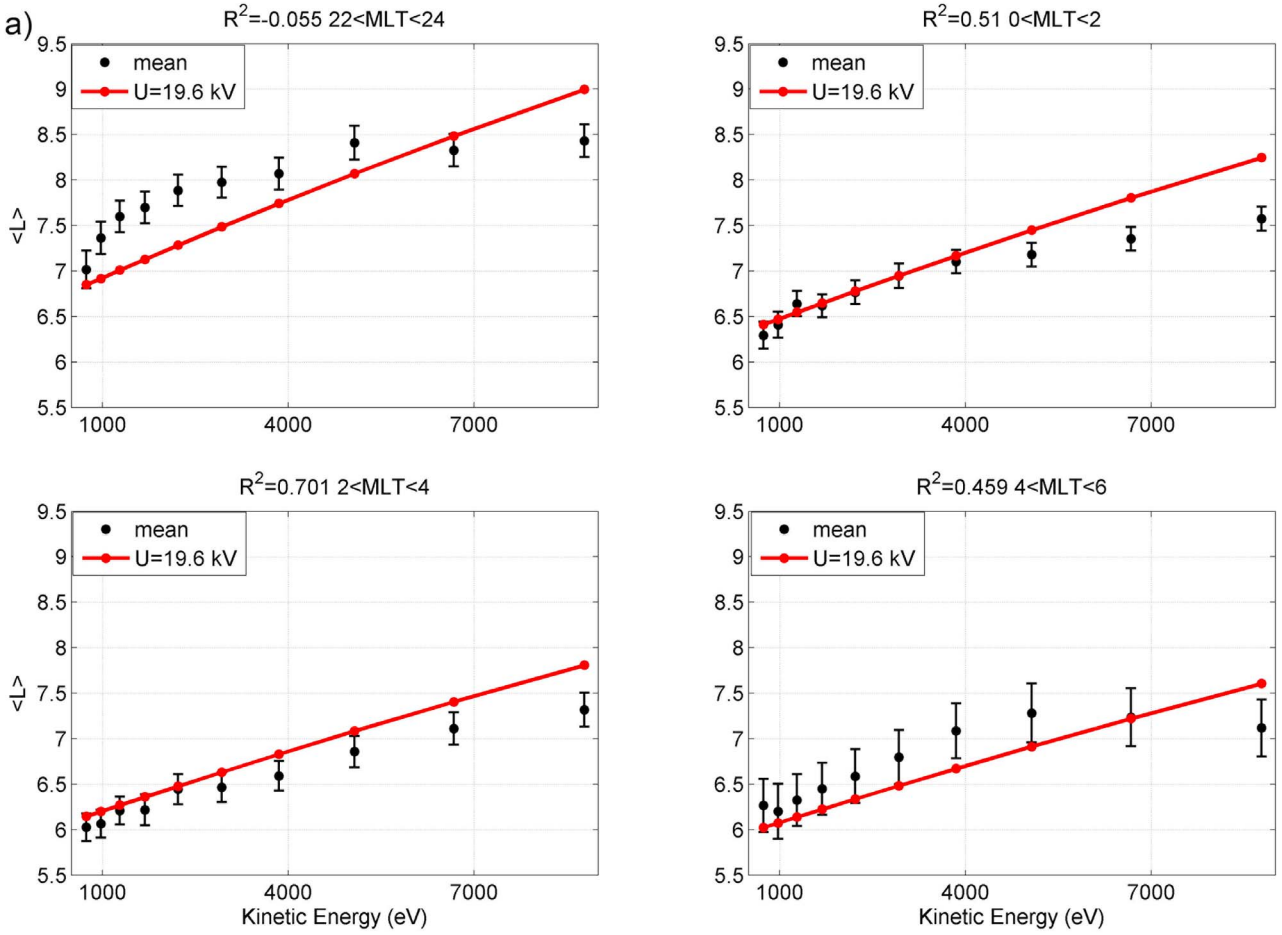

Figure 4. Equatorial radial distance of the cutoff boundary versus electron kinetic energy in eV for different levels of activity. (a) For $AE < 50$ nT. (b) Same as Figure 4a (top left), except that a green curve which represents the modeled boundary location with the same potential drop U but higher degree of shielding ($\gamma = 3.6$) is plotted on top of the red curve. (c) For 50 nT $< AE <$ 300 nT. (d) For $AE >$ 300 nT. The black dots and error bars are the medians and the SEMs in each energy bin. The red solid lines represent theoretical values from the model inferred from equations (5)–(7), where $\gamma = 2.6$ and $b = U/2*12.5^{\gamma}$. The value of U and the coefficients of determination between the black dots and the red curves are indicated.

model with $\gamma = 2.6$ and the potential drop U of the convection electric field indicated at the top left of each panel. The parameters b of equation (1) us related to U by $U = 2b(12.5)\gamma$. The value of U is obtained separately for each activity level ($AE < 50$ nT, 50 nT $< AE <$ 300 nT, and $AE >$ 300 nT) from a least squares fit to the means of L versus energy in all the local time sectors.

[18] In order to characterize the goodness of our model prediction, we use a "coefficient of determination" to measure the discrepancy between the model and observation. The definition of "coefficient of determination" is the following:

$$R^2 = 1 - \frac{\sum_{i=1}^{n}\left(y^i_{\text{obs}} - y^i_{\text{model}}\right)^2}{\sum_{i=1}^{n}\left(y^i_{\text{obs}} - \overline{y_{\text{obs}}}\right)^2},$$

where y_{obs} is the observed value, y_{model} is the model prediction, and $\overline{y_{\text{obs}}}$ is the mean of observation. The numerator is essentially the residual between the model and the data. The denominator is the deviation of the observation from its mean. The coefficient of determination represents the proportion of variability in a data set that is accounted for by the model. The value of R^2 varies from $-\infty$ to 1. $R^2 = 0$ indicates that the model predictions are only as accurate as the mean of the observed data. $R^2 = 0.5$ or higher implies that the model accounts for a substantial part of the variation of data. The closer R^2 is to 1, the more accurate the model is. When the relationship between two variables in the observation is linear and the model is obtained through linear regression, R^2 equals the square of the correlation coefficient between the observed and modeled (predicted) data values. We calculate the coefficients of determination and their values are shown at the top of each panel.

[19] In Figure 4a where the geomagnetic conditions is relatively quiet ($AE < 50$ nT), the modeled radial distance of the cutoff boundary increases as the measured electron kinetic energy of the boundary increases in each of the local time

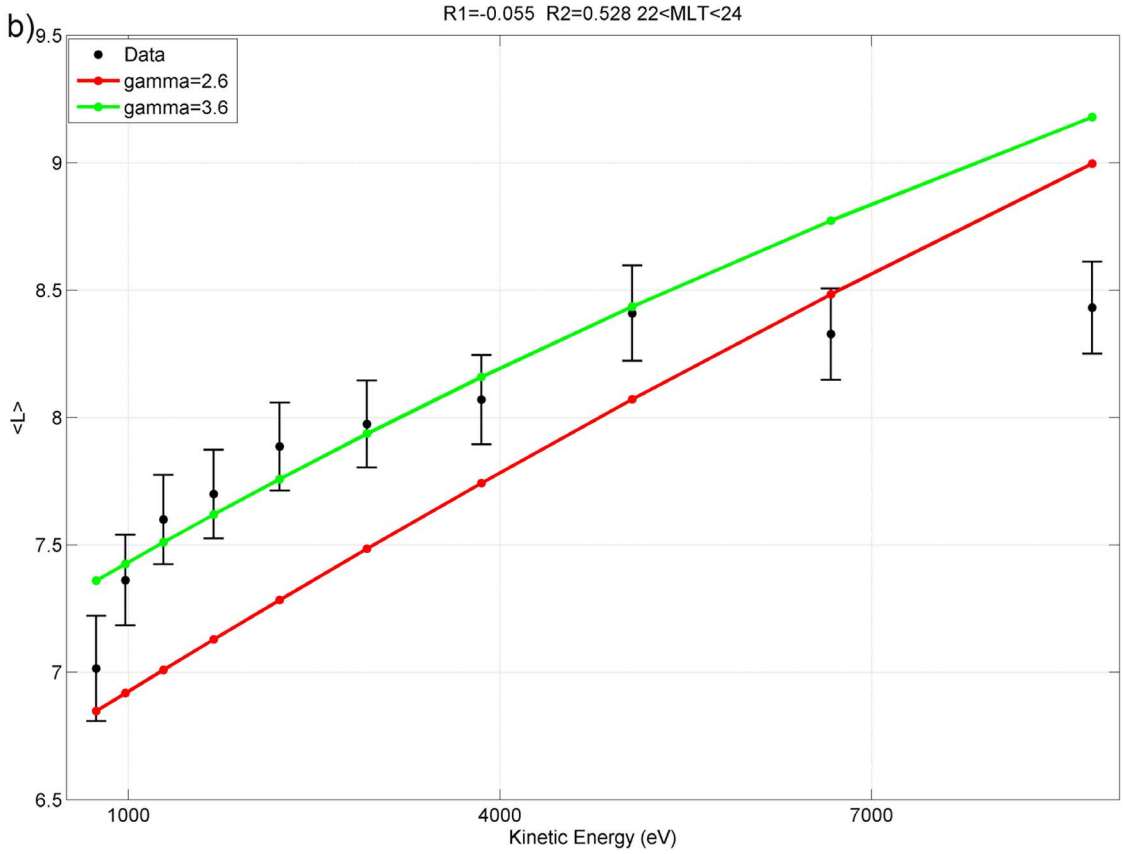

Figure 4. (continued)

bins, and the model organizes the trend of the data fairly well in all local time sectors except the premidnight sector (the coefficient of determination is ~0.5 in the postmidnight sectors and slightly less than 0 from 22:00 to 24:00 MLT). This can be accounted for if the degree of shielding in the premidnight region is larger than $\gamma = 2.6$. To illustrate this point, Figure 4b is a plot of the radial location of the cutoff boundary versus electron kinetic energy between 22:00 and 24:00. Black dots are the data; the red curve and the green curve represent the modeled location of the boundary with the same potential drop across the tail ($U = 19.6$ kV) but different degrees of shielding. One can see that a drift boundary model with $\gamma = 3.6$ fits the data better than the one with $\gamma = 2.6$. This suggests that the shielding factor may be a function of local time, a matter to which we return later in the paper. However, in Figures 4c and 4d we continue to assume $\gamma = 2.6$ in all local time sectors. In addition, the model systematically overestimates the separation in radial distance between the cutoff boundary of the highest-energy electrons and the lowest-energy electrons for the energy range we considered. This could be a result of the simplified electric field model we use, which will be discussed in section 6.

[20] Figures 4c and 4d correspond to moderately disturbed times (50 nT < AE < 300 nT) and highly disturbed times (AE > 300 nT), respectively. The data show that at such times, cutoff boundaries of different energies move closer to the Earth and the separation between the boundary of the lowest-energy electrons and that of the highest-energy electrons becomes smaller. However, the energy dispersion that one expects is not observed at such times. Indeed, in the local time region between 02:00 and 06:00 in Figures 4c and 4d, the cutoff boundaries of the lower-energy electrons are encountered outside the boundaries of the higher-energy electrons, and the cutoff boundaries of ~9 keV electrons and of ~1 keV electrons fall at almost the same radial distance. The values of the coefficients of determination indicate the model captures the trend of the data in the premidnight sector but fails to reproduce the observation in the postmidnight sectors at disturbed times. This is probably because at a high level of activity, dynamic injections become the dominant mechanism of plasma transport, and they may even produce energy dispersion signatures inverse of a convection boundary [*Mauk and Meng*, 1983]. Besides, in Figures 4c and 4d, the "abnormal" energy dispersion feature of the boundary is most evident from 02:00 to 06:00 MLT whereas from 22:00 to 24:00 MLT, the inner edge maintains the energy dispersion feature of a convection boundary despite enhanced geomagnetic activity. This could be explained if the sources of the dynamic injections are located in the midnight meridian or slightly post midnight. In this case flux cutoffs resulting from injection are observed in the postmidnight sector as the injected electrons drift counterclockwise toward the dayside. Furthermore, dynamical changes of the magnetic field are probable during times of enhanced geomagnetic

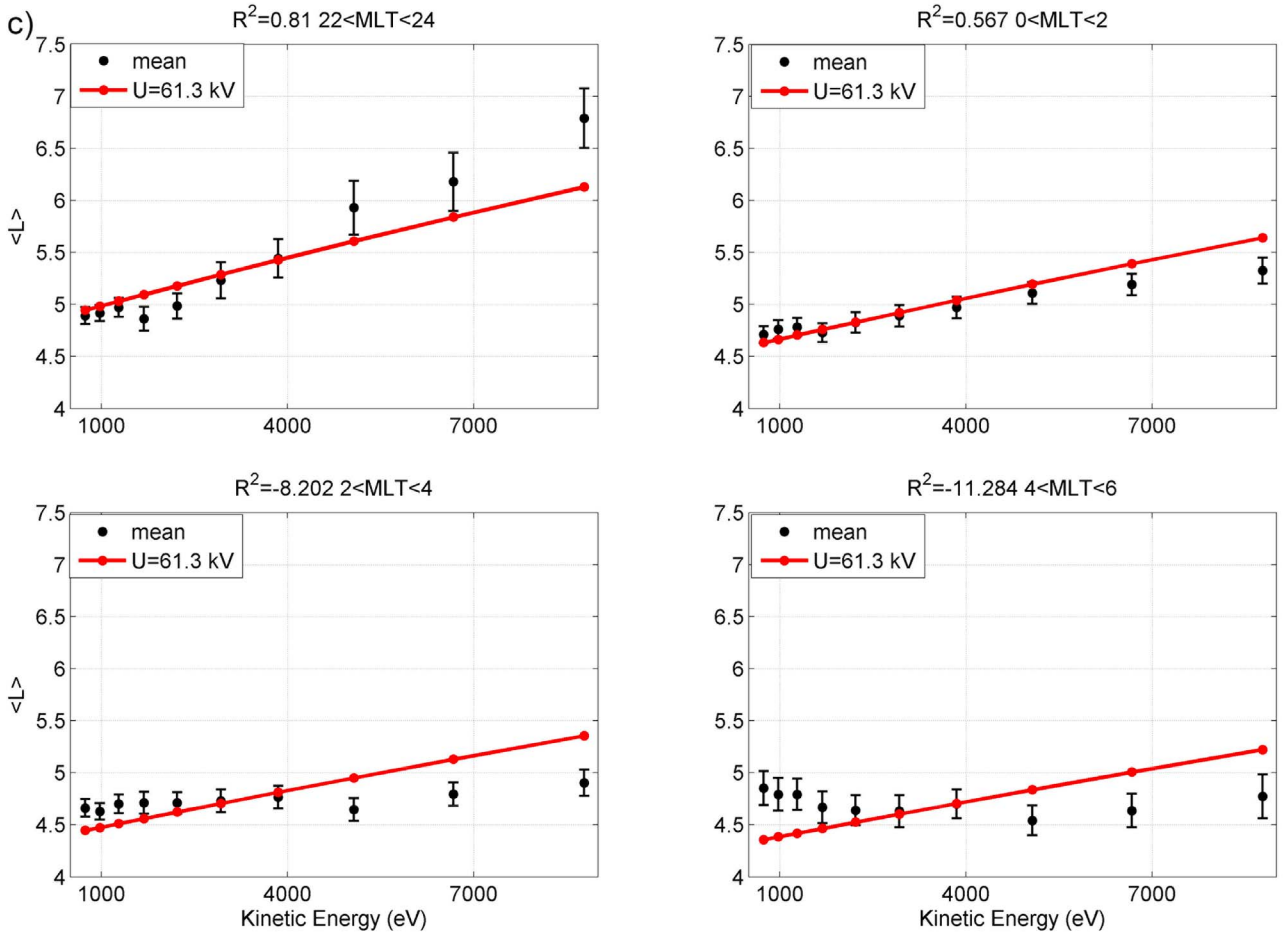

Figure 4. (continued)

activity, and acceleration mechanisms not contemplated in a static field configuration can significantly modify the distributions encountered near the inner edge of the plasma sheet.

4.2. Dependence of the Boundary Location on the Solar Wind Electric Field

[21] It has been well established that nightside electron flux cutoff boundary depends on geomagnetic activity. As the magnetosphere becomes more dynamic, the convection electric field magnitude increases and the separatrix that corresponds to the inner edge of the plasma sheet lies near the radial distance where gradient and curvature drifts may begin to dominate. Figure 5 displays the equatorial radial distance of the inner boundary of 1.7 keV electrons identified from the THEMIS data versus solar wind electric field E_y at different MLTs between 22:00 and 06:00. Here we use the cutoff boundary of 1.7 keV as representative of all energy bins, since ~1.7 keV is a typical energy of plasma sheet electrons. We obtain similar relationships between the electron cutoff boundaries and the solar wind electric field for the other 9 energy bins. To obtain E_y we use solar wind data from the ACE satellite, appropriately time shifted to the nose of the magnetopause. From the time series of u_x and B_z, we evaluate $E_{y,i}$ for each of the N data points. Retaining only those samples for which $E_{y,i} > 0$, we define the average solar wind electric field as $E_y = 1/N\sum_i (E_{y,i} > 0)$ where the summation is carried out over the N data points in the 20 min prior to the time of the crossing of the plasma sheet boundary ($N = 20$). By taking only the net $+E_y$ into account we neglect the effect of northward IMF on tail convection. In section 5.1, we discuss the reason for selecting 20 min as the averaging interval. In Figure 5a, blue circles are the data, binned by E_y, and the black crosses represent the means of E_y and L (equatorial radial distance of the inner boundary of 1.7 keV electrons). The horizontal and vertical error bars represent the SEMs of solar wind E_y and L in individual bins, respectively. Figure 5b shows distribution of data in E_y bins. We select the E_y bins so that the distribution of data points are roughly even except in the first bin ($E_y < 0.1$ mV/m). The red dashed curve in Figure 5a is obtained from the drift boundary model with $\gamma = 2.6$ and $b = (25.49E_y + 27.26)/2*12.5^{\gamma}$. This set of parameters is obtained from a least squares fit to the entire data set with b as a linear function of E_y (the details are discussed in section 5.1). The trend of the data is partly captured by the model, with L falling with increasing solar wind Ey, sharply at first and much more slowly later. The coefficients of determination between the observed L (the black crosses) and the modeled L (the red trace) for data points where $E_y < 2$ mV/m are indicated at the top of each plot in Figure 5a. The coefficient of determination is the highest in the premidnight sector and decreases toward the dawn side. This is consistent with Figures 4a, 4c, and 4d, as the model is

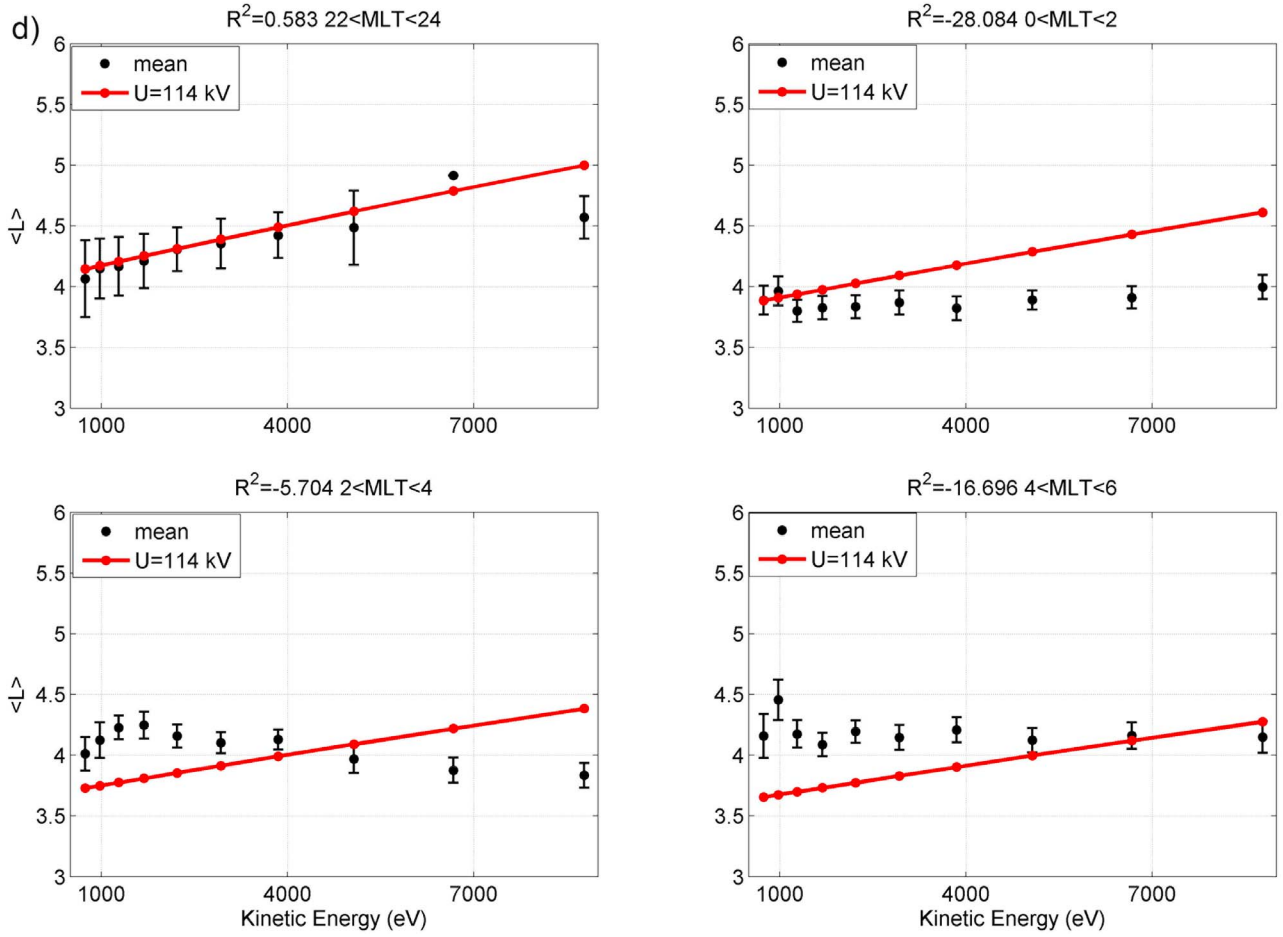

Figure 4. (continued)

most consistent with observation in the postmidnight sector during quiet times and most consistent with observation in the premidnight sector during active times. The model in general is not very good in predicting observations here, indicating the steady state drift boundary model is not accurate at times of dynamic activity.

4.3. The Inner Boundary on the Equatorial Plane

[22] Combining the results obtained in the preceding sections, Figure 6 illustrates the locus of the inner edge of the electron plasma sheet on the nightside in the equatorial plane at quiet times (AE < 50 nT on the left) and disturbed times (AE > 300 nT on the right), respectively. The green (blue) crosses and curves in Figure 6 refer to the inner boundary of ~7 keV electrons (~1 keV electrons). The curves of Figure 6 are obtained from the model of equations (5)–(7) for $\gamma = 2.6$ and $U = 20.6$ kV (Figure 6, left) and $U = 102$ kV (Figure 6, right). The values of the potential drop of the convection electric field are obtained from a least squares fit to the data in each plot of Figure 6 only; that is, they are the parameters that minimize $\chi^2 = \Sigma[L(U/2R_{mp}^2, W, \mathrm{LT}) - L]^2$.

[23] The data displayed here confirm key features of the local time asymmetry of the inner edge of the electron plasma sheet: the inner boundary lies farther outward in the premidnight sector than it does near dawn. The reason is that electrons of identical μ located at the same radial distance in a dipole field have larger azimuthal drift speed, near dawn, where their co-rotation velocity, gradient drift velocity and the azimuthal component of the sunward convection all point eastward, than in the premidnight sector, where the azimuthal component of the sunward drift opposes gradient drift and co-rotation. Thus, it takes longer in the premidnight sector than near dawn for the electrons of the same μ at the same radial distance to sweep across an hour of MLT. Meanwhile, the radial component of the sunward drift velocity is the same for electrons near dawn and near dusk. Thus, the electrons in the premidnight sector dwell for long enough to experience a larger radial displacement than the ones near dawn. Consequently, for electrons of fixed μ, the drift boundary lies farther outward in the premidnight sector than near dawn. Since $W = \mu B$ for equatorially mirroring electrons and the contours of constant B of a dipole field are circles, the local time asymmetry of the drift boundary of electrons with constant W is similar to that of electrons drifting at constant μ.

5. Variation of the Convection Electric Field With Geomagnetic Activity

[24] Typically, the convection electric field is small at quiet times and increases significantly at disturbed times [*Thomsen et al.*, 2002]. The convection strength, b, can be inferred from the model once the location of the cutoff boundary, the

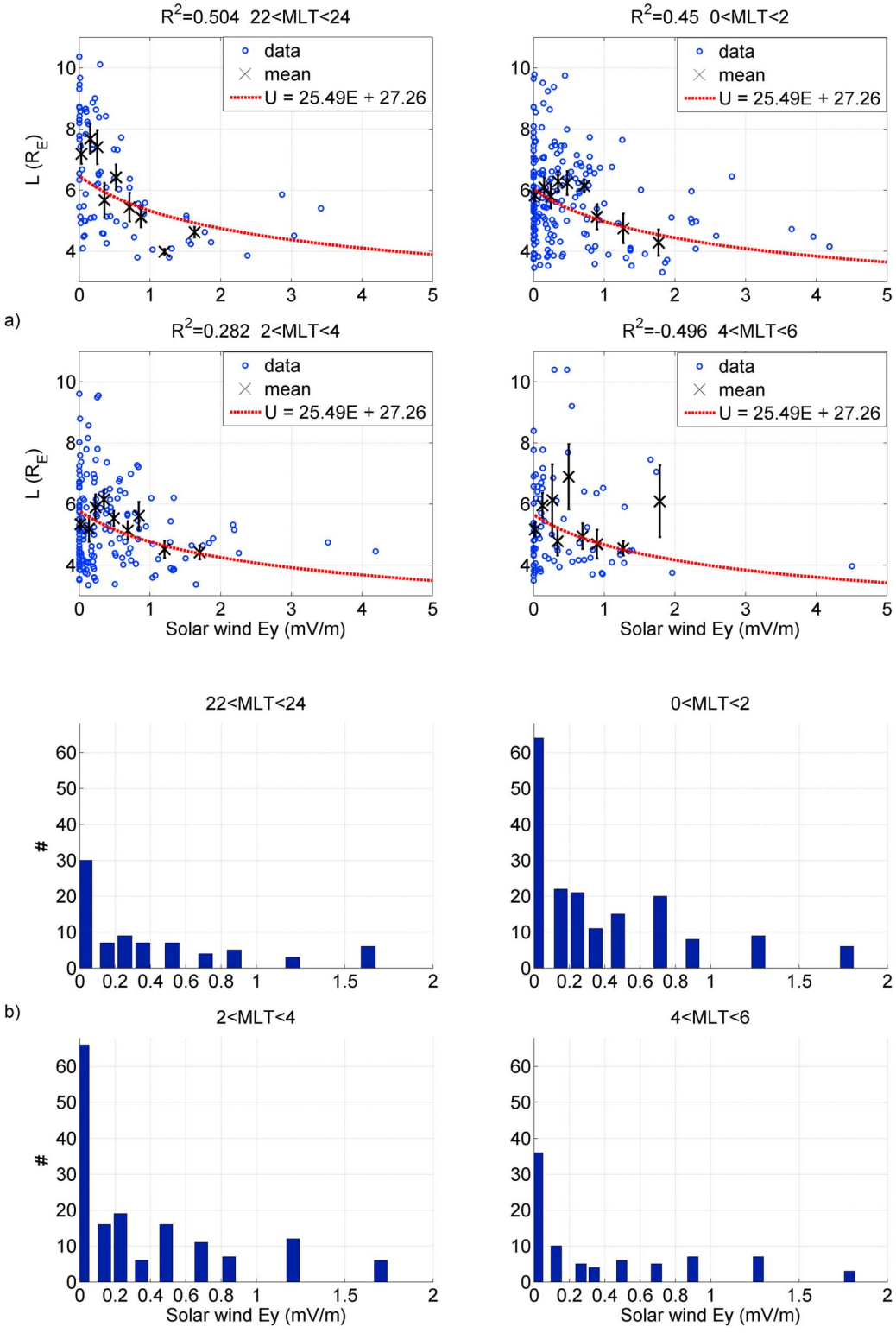

Figure 5. (a) Equatorial radial distance of the cutoff boundary versus averaged solar wind electric field E_y (see text for definition of the average) for 1.7 keV electrons. Individual graphs correspond to different local time sectors from 22:00 to 06:00 MLT. Blue open circles are the data. Black crosses are the means of E_y and L in each bin. Black error bars are the SEMs of L in each bin. We do not calculate means and error bars for $E_y > 2$ mV/m because data points are scarce in this interval and therefore highly uncertain. The red dashed line represents the theoretical value of cutoff boundaries by setting $\gamma = 2.6$ and $b = (27.26 + 25.49E_y)/2*12.5^{\gamma}$. The coefficients between the black crosses and red curves are indicated at the top. (b) Events number binned by the averaged solar wind electric field E_y.

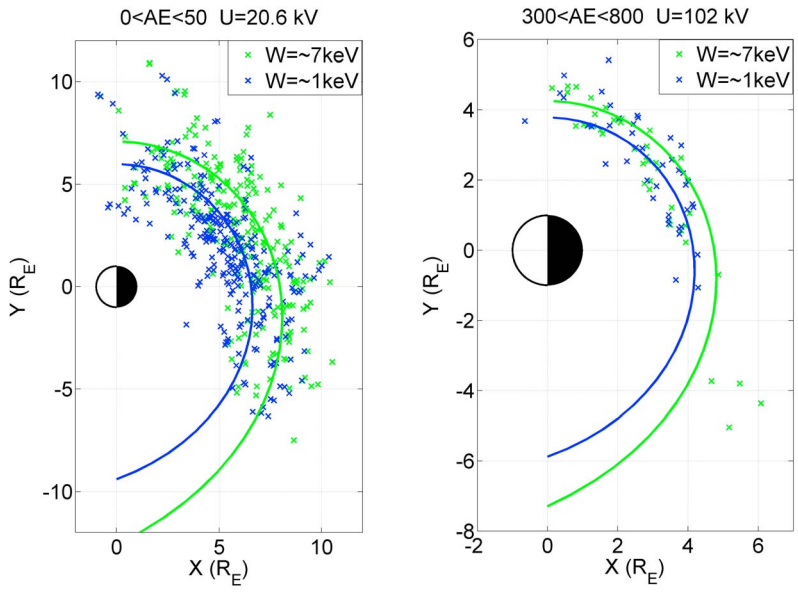

Figure 6. (left) The nightside cutoff boundaries of 90° pitch angle electrons ($\nu = 3.0$ in equation (7)) on the equatorial plane for $AE < 50$ nT. Blue and green represent inner boundaries of ~1 keV electrons and ~7 keV electrons, respectively. The crosses are taken from observations. The curves correspond to the boundaries calculated from the drift boundary model where $\gamma = 2.6$ and $U = 20.6$ kV. The value of U is obtained from a least squares fit to the crosses. (right) Same as Figure 6 (left) but for disturbed times ($AE > 300$ nT), $U = 102$ kV.

electron's energy and γ are known. The value of the convection strength, b, is obtained from a least squares fit to the boundary crossings measured in different energies during a single spacecraft pass. The potential drop U of the convection electric field follows the knowledge of b from equation (1).

[25] With U established, it is of interest to compare its values with potential drops measured in the polar cap across the antisolar flow region that maps to the region of sunward flow in the equatorial magnetosphere. In the equatorial plane near the magnetopause, the flows are driven by viscous interactions with the flowing magnetosheath, producing a convection cell that includes a region of antisolar flow. Consequently, in estimating U, we assume that the width of the region of sunward flow is somewhat smaller than the distance between the dawn and dusk flanks of the magnetopause. For this reason, U is obtained from equation (1) as the difference between the potential at dawn and at dusk taken at distance $R^*_{mp} = 12.5\ R_E$ from the center of the Earth, i.e., ~2.5 R_E inside of the nominal magnetopause distance

$$U = U\left(R^*_{mp}, \frac{\pi}{2}\right) - U\left(R^*_{mp}, -\frac{\pi}{2}\right) = 2bR^{*\gamma}_{mp}. \qquad (8)$$

We tested the Shue formulas [*Shue et al.*, 1998] for the magnetopause width and found that the fit to the data is not improved by allowing the magnetotail width to vary. Therefore, we neglect the variation of R^*_{mp} with geomagnetic activity. The magnetopause terminator near dawn/dusk is observed at distances varying between ~10 R_E and ~25 R_E and the scale size of the low-latitude boundary layer at the flanks near dawn/dusk is of order of 3–8 R_E [*Sibeck et al.*, 1991; *Sckopke et al.*, 1981]. We select $R^*_{mp} = 12.5\ R_E$ to characterize the full width across the near-equatorial magnetotail of the region of sunward return flow, including that driven by reconnection in the tail and by viscous interaction in the boundary layer.

[26] In the following section, we display the relationship between the potential drop of the convection electric field inferred from the location of the inner edge and the level of geomagnetic activity characterized alternatively by the solar wind electric field E_y, AE, and Kp.

5.1. Potential Drop of the Convection Electric Field as a Function of the Solar Wind Electric Field

[27] Figure 7a is a plot of the potential drop of the tail convection electric field calculated from equation (8) versus the solar wind electric field E_y. E_y is evaluated over 20 min intervals prior to a boundary crossing as in section 4.2. The average of E_y for each boundary crossing measured in different energies during a single pass is taken. The data points are unequally binned by their E_y values and the distribution of data points is shown in Figure 7b. The E_y bins are selected so that the number of data points are roughly even in the range of 0.4 mV/m $< E_y <$ 3 mV/m. In Figure 7a, blue crosses represent the data; the medians of E_y and the potential drop over 25 R_E are represented by the black dots, and the vertical and horizontal error bars represent the SEMs of the potential drop and the solar wind E_y in each bin, respectively.

[28] If we assume that parallel electric fields are not very large at moderately disturbed times, then the potential drop of the convection electric field that we have calculated is expected to equal the polar cap potential drop. In previous studies, the polar cap potential drop was found to vary roughly linearly with solar wind electric field for nominal conditions but to asymptote to a constant value for large solar wind electric field. *Boyle et al.* [1997] summarized a func-

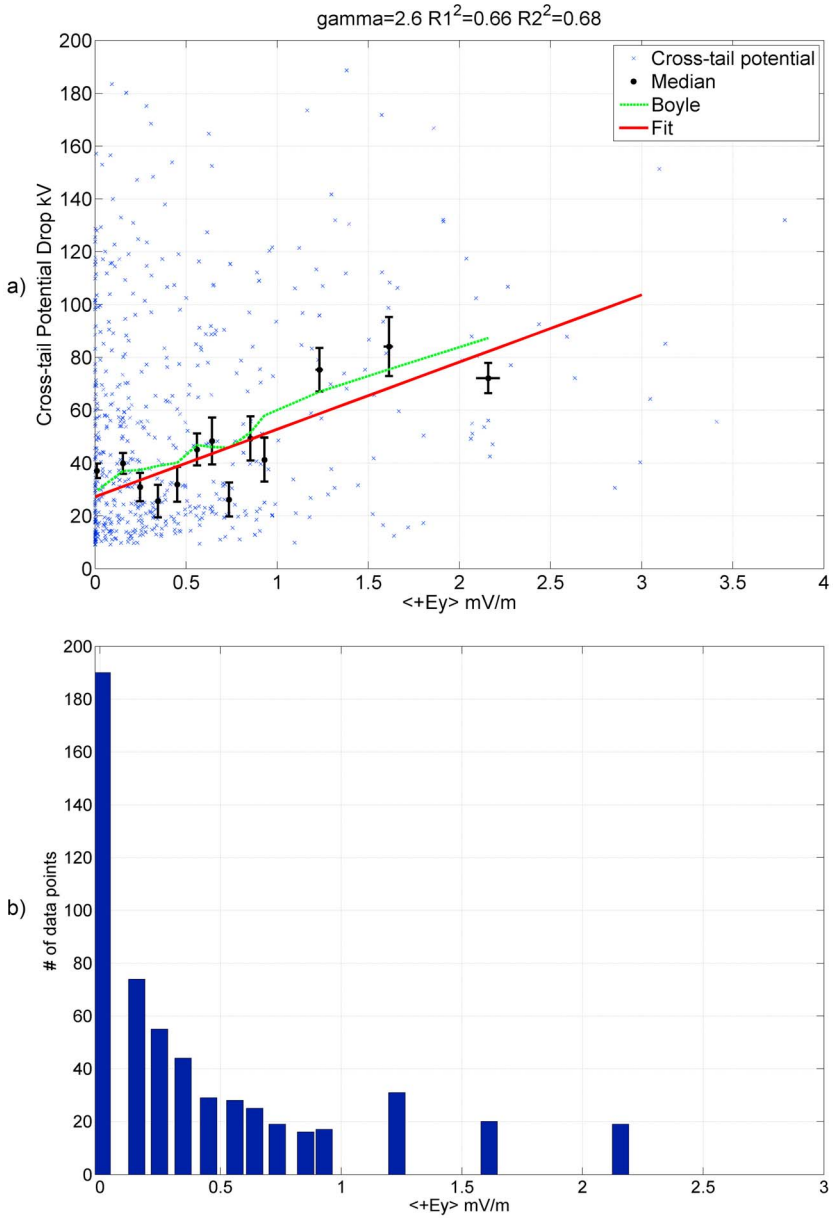

Figure 7. (a) Potential drop of the tail convection electric field versus averaged solar wind electric field E_y. Black dots are the medians of E_y and U in each bin. Horizontal and vertical error bars are the SEMs of E_y and U in each bin, respectively. The potential drop of the convection electric field is inferred from the location of the inner edge using the model of equations (5)–(7) for $\gamma = 2.6$. The red line is the linear least squares fit to the black dots for $E_y < 3$ mV/m: $U\,(\mathrm{kV}) = 27.26 + 25.49E_y$. The green curve is from equation (9) and assumes that the polar cap potential drop equals the potential drop of the earthward convective flow in the tail. (b) Events number binned by the averaged solar wind electric field E_y.

tional form of the polar cap potential drop for quasi-steady IMF (interplanetary magnetic field) conditions in the linear response regime. They suggested that

$$U_{pc}(\mathrm{kV}) = 10^{-4}u_x^2(\mathrm{km/s}) + 11.7B(\mathrm{nT})\sin^3\left(\frac{\theta}{2}\right), \qquad (9)$$

where u_x is the solar wind velocity, B is the magnitude of IMF, and $\theta = \arccos(B_z/B)$ is the angle between B_z and B in GSM coordinates. The first term in equation (9) captures the contribution to the polar cap potential drop from the antisunward flow from viscous interaction in the low-latitude boundary layer at the magnetopause flanks. The second term describes the part of the polar cap potential drop that corresponds to the earthward convective flow in the equatorial plane resulting from reconnection in the distant tail.

[29] The potential drop of the convection electric field inferred from the location of the inner edge of the electron plasma sheet in our data set can be compared with the cross polar cap potential drop predicted by equation (9) averaged

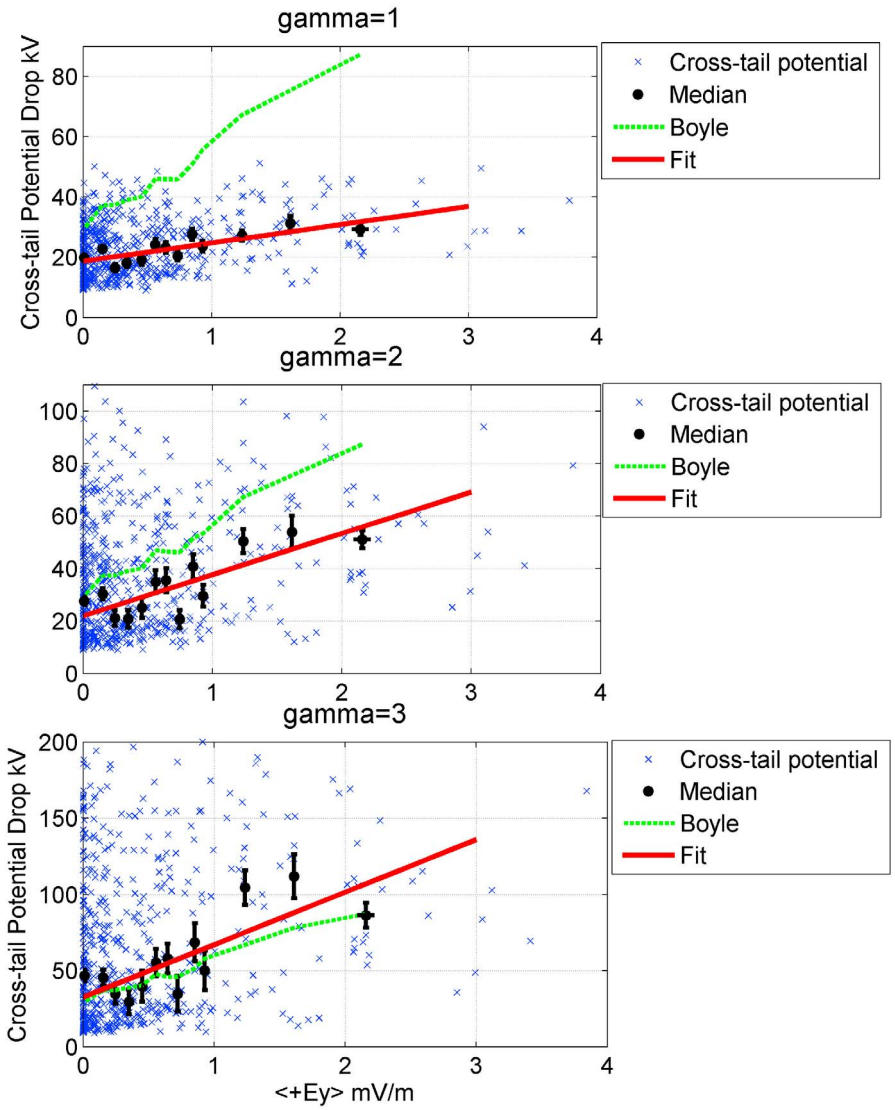

Figure 8. Same as Figure 7a, except that the shielding factor in the Volland-Stern electric potential formula is $\gamma = 1$, $\gamma = 2$, and $\gamma = 3$ from top to bottom.

over the 20 min interval prior to the boundary encounter. In Figure 7a data are binned by E_y and the medians of the polar cap potential predicted in each bin are plotted. Here the shielding factor γ in the Volland-Stern electric potential formula is set as $\gamma = 2.6$. The reason we adopt this value as the degree of shielding can be understood by examining Figure 8. The plots in Figure 8 are the same as Figure 7a for shielding factors set to $\gamma = 1$, $\gamma = 2$, and $\gamma = 3$, respectively. Equation (9) from *Boyle et al.* [1997] is also plotted. Figure 8 shows that, as the degree of shielding increases, the potential drop of the convection electric field must increase in order to leave the inner edge of the electron plasma sheet at a fixed spatial location. Moreover, when a uniform electric field model or a shielded electric field model with $\gamma = 2$ is used, the consequent potential drop of the convection electric field is smaller than the polar cap potential drop. When a shielded electric field model with $\gamma = 3$ is used, the potential drop of the convection electric field is larger than the polar cap potential. Using values from $\gamma = 2$ to $\gamma = 3$ with increments of 0.1, we find that the potential drop of the convection electric field is most consistent with the modeled values of the polar cap potential drop for $\gamma = 2.6$ (minimum difference between the black dots and the green trace).

[30] In deciding what is the appropriate time interval to use for averaging the solar wind electric field, we tested a range of averaging times as illustrated in Figure 9. Figure 9 plots the cross-magnetosphere potential drop versus the solar wind electric field averaged over different time intervals prior to the boundary encounter (10 min, 20 min, 30 min, 40 min, 50 min, and 60 min as indicated by labels). The coefficient of determination (R_1^2) between the medians of the cross-tail potential drop inferred from the measured boundary location (the black dots) and our linear fit (the red trace) and the coefficient of determination (R_2^2) between the black dots and the polar cap potential drop calculated from the Boyle formula (the green trace) are indicated at the top of each plot. We obtain the best fit as measured by R_1^2 and R_2^2 for an averaging interval of 10~20 min and 60 min. Delay times of 20 min and

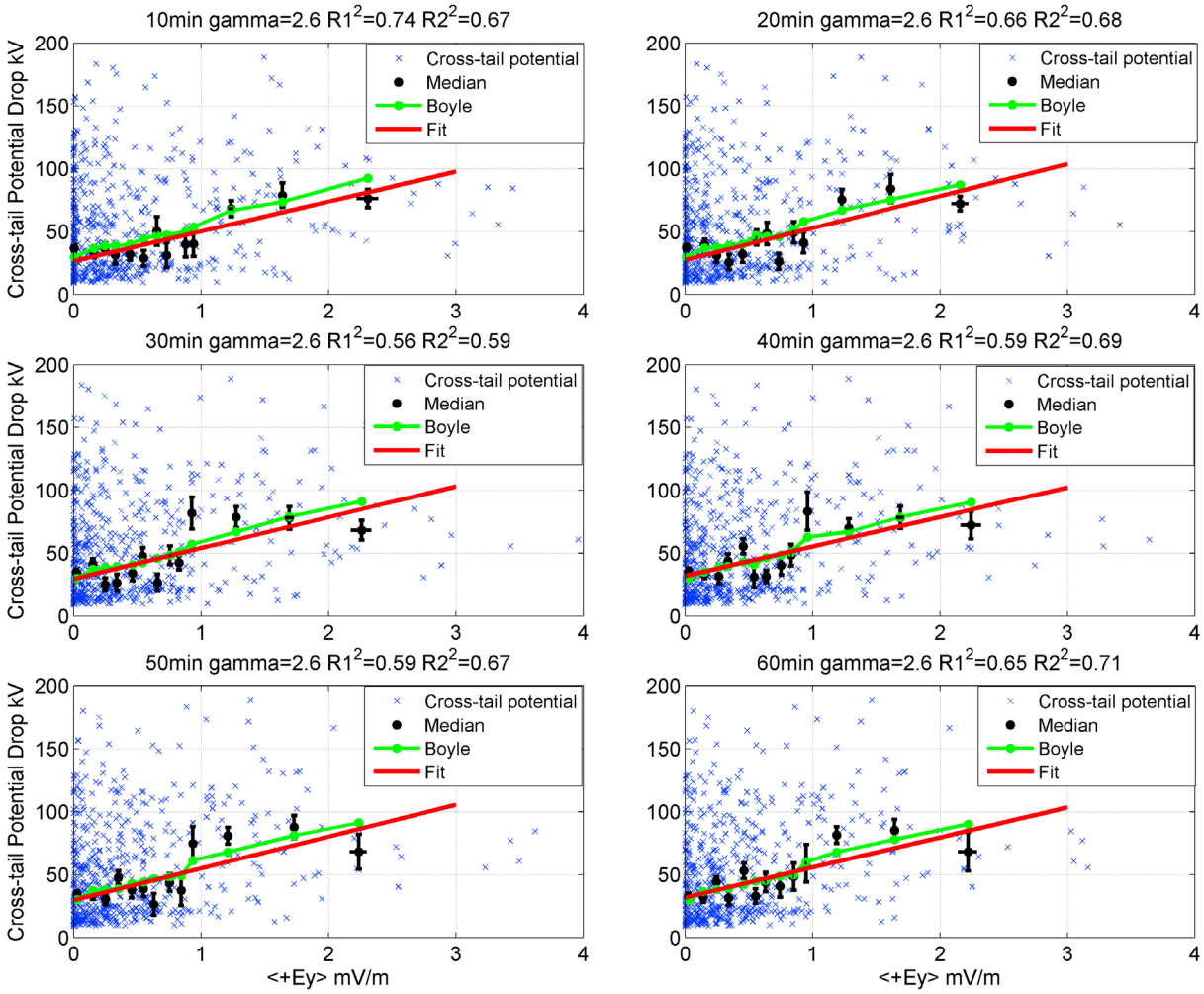

Figure 9. Cross-magnetosphere potential drop versus solar wind electric field E_y with $\gamma = 2.6$ for different time intervals of averaging the solar wind electric field (10, 20, 30, 40, 50, and 60 min, as indicated). R_1^2 is the coefficient of determination between the medians of the cross-tail potential drop inferred from the measured boundary location (black circles) and our linear fit (red line), and R_2^2 is the coefficient of determination between the black dots and the polar cap potential drop calculated from the Boyle formula (green line).

60 min have previously been reported. *Bargatze et al.* [1985] investigated the response time between the *AL* index and solar wind VB_s using linear prediction filters and found that the filters are composed of two response peaks at time lags of 20 min and 60 min. They suggested that the 20 min pulse represents magnetospheric activity driven directly by solar wind coupling (which relates directly to the convection electric field) and that the 60 min pulse represents magnetospheric activity driven by the release of energy previously stored in the magnetotail. Given the coefficients of determination we obtain here and results of previous studies, we choose 20 min as the time interval over which to average the solar wind electric field.

[31] In Figure 7a, the red trace is a least squares linear fit to the medians of the potential drop of the convection electric field inferred from the location of the inner edge (the black dots): $U(\text{kV}) = 27.26 + 25.49E_y(\text{mV/m})$. Our fit and the Boyle formula are very similar, and both the coefficients of determination R_1^2 and R_2^2 are close to 0.7. This suggests that when the solar wind electric field is small ($E_y < 1.5$ mV/m), the relationship between the driving solar wind electric field and the responsive potential drop of the tail convection electric field can be approximated by a linear formula fairly well.

5.2. Potential Drop of the Convection Electric Field as a Function of the *AE* Index

[32] The auroral electrojet indices are found to correlate with the solar wind electric field for quiet and moderately strong solar wind conditions [*Weimer et al.*, 1990]. Since the potential drop of the convection electric field is well correlated with the solar wind electric field as shown above, in this section we seek an empirical relationship between the potential drop of the convection electric field and the *AE* index. We use the provisional *AE* index averaged over 1 h prior to the cutoff boundary encounter to characterize the activity level. The potential drop of the tail convection electric field ($U_{CT} = 2bR^{*\gamma}_{mp}$, $\gamma = 2.6$) is plotted against $\langle AE \rangle$ in Figure 10. We discard data for the small number of boundary

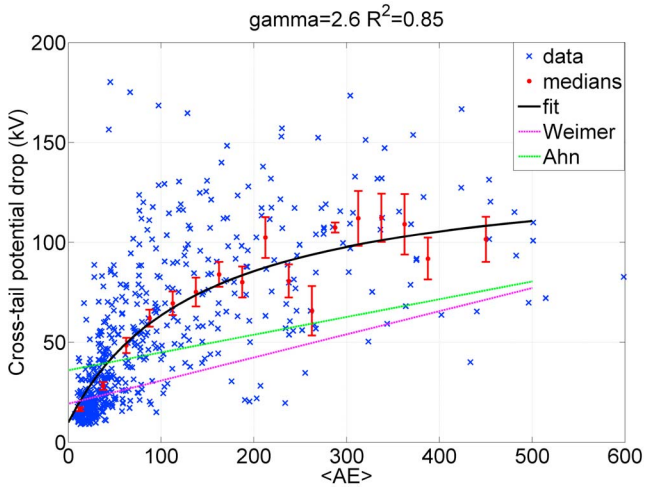

Figure 10. Potential drop of the tail convection electric field versus *AE*. Red dots and red error bars are the medians and SEMs in each bin. The black line is the least squares fit described in the text. The green and magenta curves are relationships between the cross–polar cap potential drop and *AE* estimated by *Ahn et al.* [1984] and *Weimer et al.* [1990], respectively.

crossings for which $\langle AE \rangle$ is larger than 500 and the data points are put into $\langle AE \rangle$ bins of equal increments of 25 nT. Again, U is obtained from a least squares fit to the boundary crossings measured in different energies during a single spacecraft pass. The mean of *AE* for the boundary crossings measured in the 11 energy bins during a single pass is taken as the value of *AE* for each data point. In Figure 10, blue crosses are the potential drop of the tail convection electric field inferred from the location of the cutoff boundary, red dots are the medians of *AE* and *U* in each bin, and the red error bars are the SEMs of *U* in each bin. The diameter in the *y* direction used to evaluate the potential drop is fixed at 25 R_E. We use the functional form $U_{CT}(kV) = U_0(kV) + (k*AE/C + AE)$ to fit the medians of the data: U_0 is the potential drop when $AE = 0$, which we fix at U_0 = 10 kV. *k* and *C* are free parameters in the fit. We adopt this functional form because it increases sharply with *AE* at first and flattens at higher values of *AE*, which reflects the trend of the data. The fit leads to: U_{CT} (kV) = 10 + (130*AE*/144 + *AE*). The coefficient of determination between the black dots and red trace is 0.85, indicating that our functional form captures the trend of the data.

[33] We compare our parameterization with models from observational bases of the polar cap potential drop as a function of *AE* in Figure 10. *Ahn et al.* [1984] have shown that the relationship between the polar cap potential and the *AE* index is approximately linear: Φ_A(kV) = 36 + 0.089*AE*. Similar results were obtained by *Weimer et al.* [1990] using DE 2 satellite measurements of the polar cap potential drop: Φ_w (kV) = 19.2 + 0.116*AE*. In Figure 10, the magenta curve represents Φ_W (kV) = 19.2 + 0.116AE, the functional form proposed by *Weimer et al.* [1990]. The green curve is the expression obtained by *Ahn et al.* [1984]: Φ_A (kV) = 36 + 0.089*AE*. Our parameterization gives an estimation of the cross polar cap potential drop larger than those estimated by both *Weimer et al.* [1990] and *Ahn et al.* [1984]. It also deviates from a linear relationship even for relatively low values of *AE*, a result that suggests that factors other than *AE* dominate the control of the potential drop.

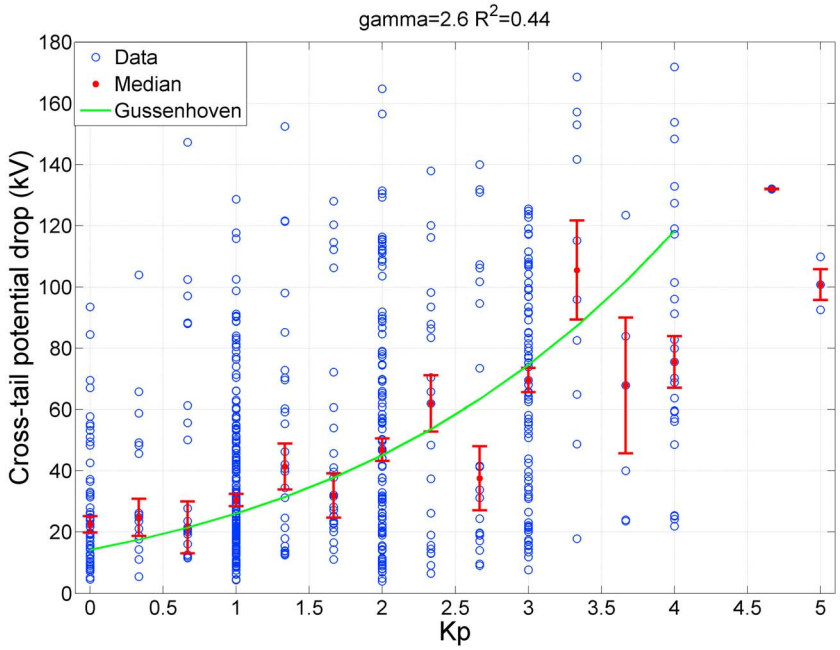

Figure 11. The potential drop of the tail convection electric field versus *Kp*. Red dots and error bars are the medians and SEMs in each *Kp* bin. The green curve is the empirical functional form proposed by *Gussenhoven et al.* [1981].

5.3. Potential Drop of the Convection Electric Field as a Function of the *Kp* Index

[34] Many studies have found that the convection electric field is well correlated with the *Kp* index. Here we investigate the relation between *Kp* and the convection electric field strength and use our data set to validate previously proposed parameterizations. In early studies, *Gussenhoven et al.* [1981] argued that the inner edge of the electron plasma sheet maps to the equatorward boundary of the diffuse aurora. From a large body of DMSP measurements, they obtained the empirical relationship between b and Kp for arbitrary values of γ:

$$b = \frac{92.4}{\gamma\left(1+\frac{1}{\gamma}\right)^{\lambda+1}}\left(\cos^2(67.8 - 2.07Kp)\right)^{\gamma}.$$

Once b is known, the potential drop of the convection electric field is obtained from $U = 2bR^{*\gamma}_{mp}$ and its relation to Kp is plotted in Figure 11. The Kp index here varies from 0 to 5 with increments of 1/3. U is obtained from a least squares fit to the mean locations of boundary crossings measured in different energies during a single spacecraft pass. The red dots and the red error bars are the medians and the SEMs in each Kp bin. The green curve is the relation proposed by *Gussenhoven et al.* [1981]. The coefficient of determination between the green trace and the red dots for $Kp < 4$ is $R^2 = 0.44$. The Gussenhoven model captures the trend of the data but scatter is very large.

[35] By comparing our fits to the dependence of the convection potential on the parameters E_y, the Kp index and the AE index in Figures 7a, 10, and 11, we find better correspondence with earlier observations for control by the solar wind electric field E_y and the Kp index than for control by the AE index. This suggests that the cross-tail convection electric field strength is more closely linked to the solar wind electric field E_y or the Kp index, than to the AE index, which essentially measures the strength of the auroral electrojets in the ionosphere and is not well correlated with convection strength in the tail.

6. Discussion and Conclusions

[36] In this study, we have used THEMIS ESA plasma data from November 2007 to April 2009 to identify the inner edge of the electron plasma sheet and investigate how its location varies with electron kinetic energy, geomagnetic activity and MLT. The comparison between our statistical results and a steady state drift boundary model with a dipole magnetic field and Volland-Stern electric field with shielding shows that, for appropriately selected parameters, the model gives a fairly good estimation of the average location of the inner boundary of the electron plasma sheet in the energy range from 0.7 keV to 9 keV and reflects the trend of the displacement of the inner edge with changing solar wind electric field at geomagnetically quiet and moderately disturbed times. However, the model cannot reproduce the energy dispersion seen at the inner edge of the electron plasma sheet at disturbed times.

[37] Since THEMIS has provided the most comprehensive and direct multipoint measurements of the inner plasma sheet so far, it is interesting to compare results of our work with previously published results. The gross features of our inner edge are consistent with early studies [e.g., *Frank*, 1971] in the sense that the locations of the inner edge of low-energy electrons typically lie inside those of high-energy electrons, and the inner edge moves earthward as activity level increases. Moreover, *Kerns et al.* [1994] found more cases of agreement between actual and convection boundaries of electron plasma sheet on the nightside during periods of decreasing activity, which is also true for our data set (Figures 4a–4d and 5). As to more recent work, *Korth et al.* [1999] showed that the statistical boundaries of higher-energy channels (~10 keV) are best fit by a Kp-dependent $\gamma = 3$ Volland-Stern electric field model whereas the electric field model with a smaller shielding factor provides a better match at lower energies (~1 keV). Therefore, they suggested that the shielding factor γ may be energy dependent. We find in our data set that by decreasing the degree of shielding with energy, the observation can be better fit by the model at geomagnetically quiet times. However, it is physically unclear how the convection potential can depend on particle energy.

[38] Several possibilities can lead to discrepancies between the model and observations shown in Figures 4a–4d and 5. At quiet times (Figure 4a), the observed distances between the electrons' inner boundaries of different energies are always smaller than predicted by the model. One way to decrease the separation is to introduce an electric field model where the gradient of the convection strength increases more sharply as a function of L than does the Volland-Stern potential. In this case, electrons with relatively high energy would penetrate closer to the Earth than they do in a Volland-Stern potential because of larger earthward drift velocities at larger L shells. Moreover, the idealized assumption of a dipolar magnetic field becomes inaccurate at $L > \sim 6\ R_E$ because it does not include effect of the tail current sheet which significantly changes the magnetic field configuration and influences particle drift motion as is evident from equations (5)–(7). It would be interesting to see whether more realistic field models can do a better job of reproducing the observations, but such analysis is beyond the scope of this paper.

[39] We have used the average locations of the inner edge of the electron plasma sheet to deduce the potential drop of the convection electric field and organized this potential by the solar wind electric field E_y. We find that despite considerable scatter in our data, with a shielded cross-tail electric field model ($\gamma = 2.6$), the inferred potential drop of the tail convection electric field are reasonably approximated by a linear relationship, and it is consistent with the *Boyle et al.* [1997] linear response model of the polar cap potential drop.

[40] The considerable discrepancies between the modeled properties (boundary locations and cross-magnetosphere potential drops) and the observations during intervals of substantial activity (see, for example, Figure 4d) reflects inaccuracies of the field models and also the neglect of temporal variations. A rapidly changing magnetic field not only modifies flow patterns but also accelerates particles, thereby changing distribution functions in ways not allowed for in our analysis. It is probable that such dynamical changes are responsible for inverting the order of boundaries at different energies at high levels of activity. Bounce-averaged energy change is proportional to energy, so the neglect of particle acceleration through temporal variations affects the higher-energy channels more than the lower-energy channels and

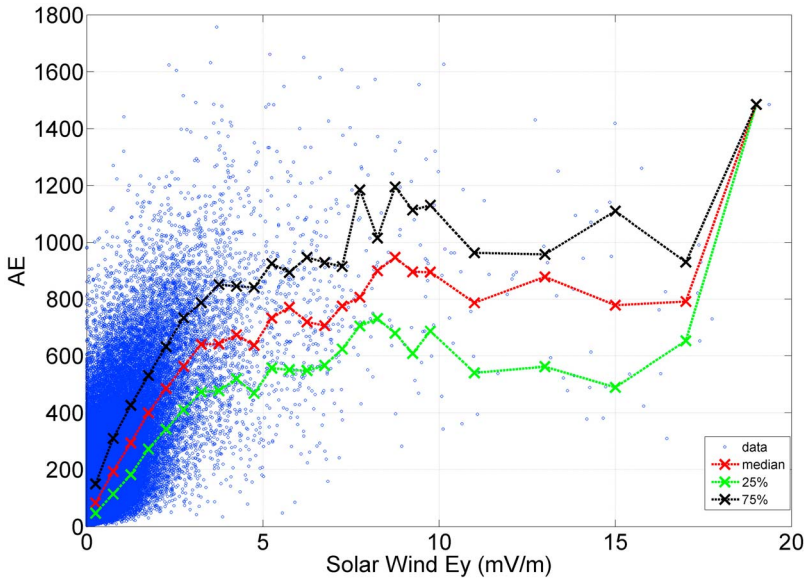

Figure 12. *AE* versus solar wind E_y from 1998 to 2009. Both *AE* and E_y are averaged over 1 h, as described in the text. Quartiles (25%, 50%, and 75%) are represented by different colors. The relation between *AE* and E_y is linear for $E_y < 4$ mV/m.

may account for a portion of the breakdown of the model for the high-energy channels in Figure 4a.

[41] During the time period of this study (from November 2007 to April 2009), the solar cycle was near minimum and large magnetic storms have not occurred, so the range of $+E_y$ is limited to $Ey < 3$ mV/m as shown in Figures 4a–4d and 6, with little data in the range from 1.5 to 3 mV/m. The restriction of the range of solar wind parameters in this study precludes an investigation of possible saturation of the potential drop of the tail convection electric field for large values of the solar wind electric field. At times other than solar minimum, solar wind electric fields attain values substantially greater than 3 mV/m. Figure 12 is a plot of *AE* versus the solar wind electric field E_y for the last solar cycle (from 1998 to 2008). Both *AE* and E_y are 1 h averaged values. Figure 12 indicates that *AE* increases linearly with E_y from 0 to 4 mV/m and continues to increase at a lower rate until E_y reaches 9 mV/m. Studies have shown that the polar cap potential drop also asymptotes to a constant value for large solar wind electric field (~10 mV/m). If we view *AE* as the ionospheric response to the driving solar wind electric field, and assume that both the magnetosphere and ionosphere respond similarly to the solar wind under extreme conditions, we conclude from Figure 12 that our data set lacks values of solar wind electric field large enough to drive the system into saturation. As solar wind conditions are likely to change in the coming years of a new solar cycle, data for large solar wind electric field are likely to become available. Such data would be desirable in order to test whether the cross-tail convective electric field saturates as the solar wind electric field reaches high levels.

[42] **Acknowledgments.** This work was supported by the NASA THEMIS funding 443869-TM-22620. Helpful suggestions from J. P. McFadden are gratefully appreciated. We thank James Weygand for providing us with solar wind data. THEMIS is made possible by NASA NAS5-02099. We thank J. McFadden for the use of the data from the ESA instrument and U. Auster, K. H. Glassmeier, and W. Baumjohann for use of the data from the FGM instrument. The FGM team acknowledges support from DLR contract 50 OC 030.

[43] Masaki Fujimoto thanks the reviewers for their assistance in evaluating this paper.

References

Ahn, B. H., S. I. Akasofu, Y. Kamide, and J. King (1984), Cross-polar cap potential drop and the energy coupling function, *J. Geophys. Res.*, *89*(A12), 11,028–11,032, doi:10.1029/JA089iA12p11028.

Alfvén, H., and C. G. Falthammar (1963), *Cosmical Electrodynamics*, Oxford Univ. Press, New York.

Angelopoulos, V. (2008), The THEMIS mission, *Space Sci. Rev.*, *141*, 5–34.

Angelopoulos, V., W. Baumjohann, C. Kennel, F. Coroniti, M. Kivelson, R. Pellat, R. Walker, H. Lühr, and G. Paschmann (1992), Bursty bulk flows in the inner central plasma sheet, *J. Geophys. Res.*, *97*(A4), 4027–4039, doi:10.1029/91JA02701.

Angelopoulos, V., C. Kennel, F. Coroniti, R. Pellat, M. Kivelson, R. Walker, C. Russell, W. Baumjohann, W. Feldman, and J. Gosling (1994), Statistical characteristics of bursty bulk flow events, *J. Geophys. Res.*, *99*(A11), 21,257–21,280, doi:10.1029/94JA01263.

Bargatze, L. F., D. N. Baker, R. L. McPherron, and E. W. Hones Jr. (1985), Magnetospheric impulse response for many levels of geomagnetic activity, *J. Geophys. Res.*, *90*(A7), 6387–6394.

Boyle, C., P. Reiff, and M. Hairston (1997), Empirical polar cap potentials, *J. Geophys. Res.*, *102*(A1), 111–125, doi:10.1029/96JA01742.

Chen, A. J. (1970), Penetration of low-energy electrons deep into the magnetosphere, *J. Geophys. Res.*, *75*(13), 2458–2467, doi:10.1029/JA075i013p02458.

Frank, L. A. (1971), Relationship of the plasma sheet, ring current, trapping boundary, and plasmapause near the magnetic equator and local midnight, *J. Geophys. Res.*, *76*(10), 2265–2275.

Friedel, R., H. Korth, M. Henderson, M. Thomsen, and J. Scudder (2001), Plasma sheet access to the inner magnetosphere, *J. Geophys. Res.*, *106*(A4), 5845–5858, doi:10.1029/2000JA003011.

Gussenhoven, M., D. Hardy, and W. Burke (1981), DMSP/F2 electron observations of equatorward auroral boundaries and their relationship to magnetospheric electric fields, *J. Geophys. Res.*, *86*(A2), 768–778, doi:10.1029/JA086iA02p00768.

Kennel, C. F. (1969), Consequences of a magnetospheric plasma, *Rev. Geophys.*, *7*(1–2), 379–419.

Kerns, K., D. Hardy, and M. Gussenhoven (1994), Modeling of convection boundaries seen by CRRES in 120-eV to 28-keV particles, *J. Geophys. Res.*, *99*(A2), 2403–2414, doi:10.1029/93JA02767.

Kivelson, M. G., and D. J. Southwood (1975), Approximations for the study of drift boundaries in the magnetosphere, *J. Geophys. Res.*, *80*(25), 3528–3534, doi:10.1029/JA080i025p03528.

Korth, H., M. Thomsen, J. Borovsky, and D. McComas (1999), Plasma sheet access to geosynchronous orbit, *J. Geophys. Res.*, *104*(A11), 25,047–25,061.

Mauk, B. H., and C. I. Meng (1983), Dynamic injection as the source of near geostationary quiet time particle spatial boundaries, *J. Geophys. Res.*, *88*(A12), 10,011–10,024, doi:10.1029/JA088iA12p10011.

McFadden, J. P., et al. (2008), The THEMIS ESA plasma instrument and in-flight calibration, *Space Sci. Rev.*, *141*, 277–302.

Schield, M. A., and L. A. Frank (1970), Electron observations between the inner edge of the plasma sheet and the plasmapause, *J. Geophys. Res.*, *75*(28), 5401–5414.

Sckopke, N., G. Paschmann, G. Haerendel, B. Sonnerup, S. Bame, T. Forbes, E. Hones Jr., and C. Russell (1981), Structure of the low-latitude boundary layer, *J. Geophys. Res.*, *86*(A4), 2099–2110.

Shue, J.-H., et al. (1998), Magnetopause location under extreme solar wind conditions, *J. Geophys. Res.*, *103*(A8), 17,691–17,700, doi:10.1029/98JA01103.

Sibeck, D. G., and V. Angelopoulos (2008), THEMIS science objectives and mission phases, *Space Sci. Rev.*, *141*, 35–59.

Sibeck, D. G., R. E. Lopez, and E. C. Roelof (1991), Solar wind control of the magnetopause shape, location, and motion, *J. Geophys. Res.*, *96*(A4), 5489–5495.

Southwood, D., and M. Kivelson (1975), An approximate analytic description of plasma bulk parameters, and pitch angle anisotropy under adiabatic flow, in a dipolar magnetospheric field, *J. Geophys. Res.*, *80*(16), 2069–2073, doi:10.1029/JA080i016p02069.

Stern, D. P. (1975), The motion of a proton in the equatorial magnetosphere, *J. Geophys. Res.*, *80*(4), 595–599, doi:10.1029/JA080i004p00595.

Thomsen, M. F., H. Korth, and R. C. Elphic (2002), Upper cutoff energy of the electron plasma sheet as a measure of magnetospheric convection strength, *J. Geophys. Res.*, *107*(A10), 1331, doi:10.1029/2001JA000148.

Vasyliunas, V. M. (1968), A survey of low-energy electrons in the evening sector of the magnetosphere with OGO 1 and OGO 3, *J. Geophys. Res.*, *73*(9), 2839–2884.

Volland, H. (1973), A semiempirical model of large-scale magnetospheric electric fields, *J. Geophys. Res.*, *78*(1), 171–180, doi:10.1029/JA078i001p00171.

Weimer, D., L. Reinleitner, J. Kan, L. Zhu, and S.-I. Akasofu (1990), Saturation of the auroral electrojet current and the polar cap potential, *J. Geophys. Res.*, *95*(A11), 18,981–18,987, doi:10.1029/JA095iA11p18981.

Whipple, E. C., Jr. (1978), (*U*, *B*, *K*) coordinates: A natural system for studying magnetospheric convection, *J. Geophys. Res.*, *83*(A9), 4318–4326.

V. Angelopoulos, T. Hsu, F. Jiang, K. K. Khurana, M. G. Kivelson, and R. J. Walker, Institute of Geophysics and Planetary Physics, University of California, Box 951567, 595 Charles Young Dr. East, Los Angeles, CA 90095-1567, USA. (fjiang@igpp.ucla.edu)